iScience

Article

Automated comprehensive evaluation of coronary artery plaque in IVOCT using deep learning

Graphical abstract

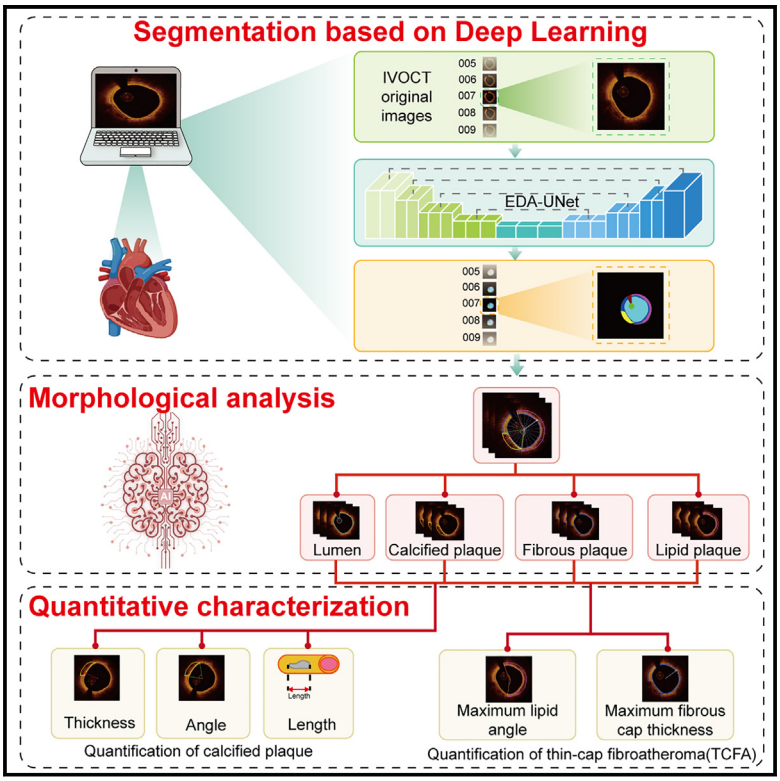

Highlights

- We developed a deep learning model for automatic characterization and quantification of IVOCT
- The model is highly correlated and consistent with the ground truth
- The model significantly reduces the time and subjectivity of manual analysis

Authors

Pengfei Liu, Zang Lu, Wenqing Hou, ..., Yitong Ma, Jianguo Dai, Xiang Ma

Correspondence

djg_inf@shzu.edu.cn (J.D.), maxiangxj@yeah.net (X.M.)

In brief

Artificial intelligence; Cardiovascular medicine

Liu et al., 2025, iScience *28*, 112169
April 18, 2025
https://doi.org/10.1016/j.isci.2025.112169

CellPress

iScience

CellPress
OPEN ACCESS

Article

Automated comprehensive evaluation of coronary artery plaque in IVOCT using deep learning

Pengfei Liu,[1,6] Zang Lu,[2,6] Wenqing Hou,[3,6] Kaisaierjiang Kadier,[1] Chunying Cui,[4] Zhengyang Mu,[3] Aikeliyaer Ainiwaer,[5] Xinliang Peng,[1] Gulinuer Wufu,[1] Yitong Ma,[1] Jianguo Dai,[2,*] and Xiang Ma[1,7,*]

[1]Department of Cardiology, First Affiliated Hospital of Xinjiang Medical University, Urumqi, China
[2]College of Information Science and Technology, Shihezi University, Shihezi 832003, Xinjiang, China
[3]School of Information Network Security, Xinjiang University of Political Science and Law, Tumxuk 843900, China
[4]Department of Emergency, Jining No.1 People's Hospital, Jining 272011, Shandong Province, China
[5]Department of Physiology, Cardiovascular Research Institute Maastricht (CARIM), Maastricht, the Netherlands
[6]These authors contributed equally
[7]Lead contact
*Correspondence: djg_inf@shzu.edu.cn (J.D.), maxiangxj@yeah.net (X.M.)
https://doi.org/10.1016/j.isci.2025.112169

SUMMARY

The process of manually characterizing and quantifying coronary artery plaque tissue in intravascular optical coherence tomography (IVOCT) images is both time-consuming and subjective. We have developed a deep learning-based semantic segmentation model (EDA-UNet) designed specifically for characterizing and quantifying coronary artery plaque tissue in IVOCT images. IVOCT images from two centers were utilized as the internal dataset for model training and internal testing. Images from another independent center employing IVOCT were used for external testing. The Dice coefficients for fibrous plaque, calcified plaque, and lipid plaque in external tests were 0.8282, 0.7408, and 0.7052 respectively. The model demonstrated strong correlation and consistency with the ground truth in the quantitative analysis of calcification scores and the identification of thin-cap fibroatheroma (TCFA). The median duration for each callback analysis was 18 s. EDA-UNet model serves as an efficient and accurate technological tool for plaque characterization and quantification.

INTRODUCTION

Coronary artery disease (CAD) is a prevalent cardiovascular condition and a leading cause of death globally.[1,2] Consequently, an accurate diagnosis of CAD is especially critical. Research has shown that, in addition to the degree of coronary artery stenosis, the complex multi-component structure of atherosclerotic plaques is equally critical.[3] The morphological and compositional characteristics of these plaques directly influence their vulnerability, which in turn differentially impacts clinical outcomes and disease progression.[4] Intravascular optical coherence tomography (IVOCT) is a catheter-based intravascular imaging modality characterized by high resolution (lateral resolution of 10–15 μm).[5] This technique provides a detailed depiction of the region surrounding the lumen of the coronary artery, including fibrous, calcified, and lipid plaques.

However, each IVOCT catheter pullback can generate 300–350 high-resolution OCT images that contain substantial vascular and plaque lesion information, rendering image annotation both challenging and time-consuming.[6] In clinical practice, IVOCT-acquired images must be expertly interpreted by clinicians, a process that is inevitably influenced by the clinicians' subjectivity and the variability of their clinical experience. Similarly, intra- and inter-observer variability, along with inter-agency reproducibility, presents significant challenges.[7] Additionally, the complex morphological characterization of plaques and the determination of quantitative indices represent significant challenges. Thin-cap fibrous atherosclerosis (TCFA) is the primary type of vulnerable plaque, characterized by a fibrous cap that is thinner than 65 μm at its thinnest point and a lipid core.[8,9] Research has demonstrated that TCFA is a significant risk factor for plaque rupture and a primary cause of acute coronary syndrome (ACS).[10] Furthermore, the extent and distribution patterns of coronary calcification indicate the progression of CAD and can predict the occurrence of adverse cardiovascular events.[11] Calcified plaque not only impairs coronary blood flow but also results in inadequate stent apposition, triggering significant interventional complications.[12] Therefore, rapid, accurate, and fully automated plaque segmentation and quantitative modeling of IVOCT images during interventional procedures are essential for intraprocedural planning and timely therapeutic decisions.

The introduction of artificial intelligence (AI) technology is anticipated to standardize and automate the segmentation and interpretation of plaque tissue in IVOCT images and to quantify

Table 1. Quantitative comparison of different models in the task of overall coronary plaque tissue segmentation

	Internal test					External test				
Models	Sensitivity	Specificity	Accuracy	MIoU	Dice coefficient	Sensitivity	Specificity	Accuracy	MIoU	Dice coefficient
U-Net	0.7286[a]	0.8758[a]	0.9869[a]	0.7861[a]	0.8667[a]	0.8467[a]	0.8476[a]	0.9837[a]	0.7431[a]	0.8424[a]
ResUNet	0.5691[a]	0.8001[a]	0.9740[a]	0.6685[a]	0.7710[a]	0.7455[a]	0.7956[a]	0.9731[a]	0.6371[a]	0.7587[a]
UNet++	0.7272[a]	0.8730[a]	0.9867[a]	0.7837[a]	0.8644[a]	0.8430[a]	0.8539[a]	0.9837[a]	0.7470[a]	0.8437[a]
AttUNet	0.7283[a]	0.8794[a]	0.9870[a]	0.7894[a]	0.8686[a]	0.8431[a]	0.8345[a]	0.9827[a]	0.7311[a]	0.8332[a]
SegNet	0.7400[a]	0.8843[a]	0.9881[a]	0.7953[a]	0.8741[a]	0.8420[a]	0.8551[a]	0.9827[a]	0.5943[a]	0.8430[a]
PSPNet	0.5638[a]	0.7216[a]	0.9715[a]	0.5993[a]	0.7105[a]	0.7214[a]	0.7189[a]	0.9733[a]	0.8227[a]	0.7160[a]
SegFormer	0.7733[a]	0.9018[a]	0.9907[a]	0.8186[a]	0.8914[a]	0.8587[a]	0.8282[a]	0.9852[a]	0.7400[a]	0.8381[a]
EDA-UNet (Ours)	0.7981	0.9067	0.9922	0.8333	0.9011	0.8620	0.8889	0.9875	0.7849	0.8689

MIoU, mean intersection over union.
[a]Comparison with EDA-UNet model, $p < 0.05$.

associated high-risk plaques. Although the application of machine learning (ML) and deep learning (DL) for characterizing coronary artery plaques in IVOCT has shown some success, certain limitations remain.[13–15] First, ML methods rely on manually crafted feature extractors and classifiers, which demand high quality and accuracy in the input data. When encountering noise interference (such as artifacts), these methods often struggle to accurately extract meaningful features, resulting in reduced image segmentation performance.[16,17] Second, most current DL-based studies primarily focus on segmenting one or two tissue types, such as fibrous tissue, lipid tissue, or calcified tissue. However, to comprehensively assess the stability of coronary artery plaques and provide more effective guidance for clinicians, it is essential to characterize and classify multiple plaque types and quantify both calcified and vulnerable plaques.[18,19] Furthermore, most existing studies develop models based on single-center, limited-scale datasets without independent external validation, thereby restricting the models' generalizability for practical clinical applications.[20]

The aim of this study is to propose a new model (EDA-UNet) for the comprehensive characterization and quantitative analysis of IVOCT image plaques based on DL semantic segmentation technology. The model was trained on a multi-center dataset reflective of real-world clinical scenarios to provide rapid, automated, and precise characterization of coronary artery plaques, as well as further quantification of TCFA and calcified plaques. Finally, we compared the performance of the EDA-UNet model with physicians with varying levels of experience in IVOCT interpretation. This study paves the way for real-time and accurate IVOCT image interpretation, which may lead to a broader application of IVOCT in CAD diagnosis.

RESULTS

Comparison between different models

In the internal test dataset, the EDA-UNet model was compared against seven state-of-the-art models. The results indicated that the EDA-UNet model outperformed all other models on evaluation metrics, particularly in the segmentation tasks of overall coronary artery plaque tissue, fibrous plaque, calcified plaque, and lipid plaque, with Dice coefficients of 0.9011, 0.8539, 0.7829, and 0.7845, respectively, surpassing the performance of other models (Tables 1, 2, 3, and 4).

In the external test dataset, the generalization capabilities of the different models varied. Notably, the EDA-UNet model continued to perform exceptionally. As shown in Tables 1, 2, 3, and 4, the proposed model excelled across all evaluation metrics for the segmentation tasks of overall coronary artery plaque tissue, fibrous plaque, calcified plaque, and lipid plaque, with Dice coefficients of 0.8689, 0.8282, 0.7408, and 0.7052, respectively, further reinforcing its position as a leading model.

In a comparison with the results reported by various models in previous IVOCT plaque segmentation studies, the EDA-UNet model demonstrated higher performance in both mean intersection over union (MIoU) and Dice coefficients (Table 5).

In addition, we evaluated the plaque segmentation performance of the EDA-UNet model on challenging IVOCT images. In complex scenarios, such as residual blood caused by incomplete flushing (Figures 1A and 1B), coronary artery dissection (Figures 1C and 1D), branch vessels (Figures 1E and 1F), and extremely eccentric catheter (Figures 1G and 1H), the proposed model effectively segmented coronary plaques. However, in certain cases, such as images containing microvessels (Figures 1I and 1J) or branch vessels that do not intersect the lumen (Figures 1K and 1L), highly attenuated regions with well-defined edges may be misinterpreted as calcified plaques, resulting in segmentation errors.

Ablation experiments

In the internal test dataset, the ablation experiment began with the baseline U-Net model (Base) of the EDA-UNet architecture. The experiment successively added the encoding feature extraction (EAFE) module, the atrous spatial pyramid pooling (ASPP) module, and the decoding feature extraction (DAFE) module. Based on sensitivity, specificity, accuracy, MIoU, and Dice coefficient metrics, the experimental results show that the EDA-UNet model demonstrated significant performance improvements with each module added to the Base model, further verifying the effectiveness and synergy of each module (Figure 2).

Table 2. Quantitative comparison of different models in the task of fibrous plaque segmentation

	Internal test					External test				
Models	Sensitivity	Specificity	Accuracy	IoU	Dice coefficient	Sensitivity	Specificity	Accuracy	IoU	Dice coefficient
U-Net	0.8417[a]	0.8145[a]	0.9918[a]	0.7048[a]	0.8261[a]	0.8392[a]	0.9924[a]	0.8192[a]	0.7069[a]	0.8280
ResUNet	0.7500[a]	0.7821[a]	0.9913[a]	0.6152[a]	0.7599[a]	0.7863[a]	0.9917[a]	0.7937[a]	0.6511[a]	0.7886[a]
UNet++	0.8527[a]	0.8052[a]	0.9912[a]	0.7051[a]	0.8264[a]	0.8211[a]	0.9920[a]	0.8116[a]	0.7055[a]	0.8270[a]
AttUNet	0.8505[a]	0.8115[a]	0.9915[a]	0.7086[a]	0.8287[a]	0.8423	0.9918[a]	0.8080[a]	0.7008[a]	0.8238[a]
SegNet	0.8365[a]	0.8200[a]	0.9922	0.7059[a]	0.8269[a]	0.8274[a]	0.9924[a]	0.8162[a]	0.6965[a]	0.8208[a]
PSPNet	0.7553[a]	0.7423[a]	0.9888[a]	0.5897[a]	0.7389[a]	0.7887[a]	0.9904[a]	0.7700[a]	0.6367[a]	0.7778[a]
SegFormer	0.8602[a]	0.8322[a]	0.9926	0.7337[a]	0.8455[a]	0.8000[a]	0.9934	0.8368	0.6677[a]	0.7997[a]
EDA-UNet (Ours)	0.8652	0.8435	0.9930	0.7465	0.8539	0.8445	0.9943	0.8470	0.7071	0.8282

IoU, intersection over union.
[a]Comparison with EDA-UNet model, $p < 0.05$.

Plaque quantification

The proposed model quantified fibrous cap thickness and lipid angle in IVOCT images from 10 pullbacks in the external test dataset by comparing the automatic measurements of the EDA-UNet model with the ground truth assessment. Pearson correlation analysis revealed a significant correlation between the model's assessment metrics and the ground truth (maximum lipid angle, r = 0.99, $p < 0.001$; minimum fibrous cap thickness, r = 0.99, $p < 0.001$) (Figures 3A and 3B). The Bland-Altman analysis showed that the bias between the model measurements and the ground truth was minimal (maximum lipid angle, −0.911 ± 6.509°; minimum fibrous cap thickness, −0.002 ± 0.011 mm) (Figures 3C and 3D).

In addition, for TCFA identification, the Phi correlation analysis revealed a strong correlation between the EDA-UNet model and the ground truth (Phi correlation = 0.691, $p < 0.001$), while the Cohen's Kappa analysis demonstrated very strong agreement (Cohen's Kappa = 0.705, $p < 0.001$). The performance of the proposed model in TCFA recognition was further evaluated through a confusion matrix with the following performance metrics: accuracy, 0.8556; specificity, 0.9388; sensitivity, 0.7561; and F1-score, 0.8267 (Figure 4).

The EDA-UNet model also evaluated comprehensive feature indicators of calcified plaques in IVOCT images, including angle, thickness, depth, and area. Pearson correlation analysis revealed a significant correlation between the proposed model's assessment indicators and the ground truth (calcified angle: r = 0.99, $p < 0.001$; calcification thickness: r = 0.95, $p < 0.001$; calcification depth: r = 0.95, $p < 0.001$; calcification area: r = 0.98, $p < 0.001$) (Figures 5A–5D). Additionally, Bland-Altman analysis indicated minimal bias between the proposed model's measurements and the true values (calcified angle: −0.262 ± 9.223°; maximum calcification thickness: 0.018 ± 0.134 mm; average deviation in calcification depth: −0.003 ± 0.051 mm; average deviation in calcification area: 0.032 ± 0.381 mm^2) (Figures 5E–5H).

In the quantitative evaluation of the calcification score, Spearman correlation analysis revealed a strong correlation between the EDA-UNet model and the ground truth (r = 0.940, $p < 0.001$), while weighted Kappa analysis demonstrated a high degree of agreement (weighted Kappa = 0.858, $p < 0.001$). The classification performance of the calcification score was assessed using a confusion matrix (Figure 6). The proposed model demonstrates outstanding accuracy and robustness, achieving an accuracy of 0.8966, a specificity of 0.9708, a sensitivity of 0.9009, and an F1-score of 0.9110.

Comparison of the EDA-UNet model with clinicians

In a reader study from the external dataset, the EDA-UNet model demonstrated superior performance to clinicians in overall

Table 3. Quantitative comparison of different models in the task of calcified plaque segmentation

	Internal test					External test				
Models	Sensitivity	Specificity	Accuracy	IoU	Dice coefficient	Sensitivity	Specificity	Accuracy	IoU	Dice coefficient
U-Net	0.6864[a]	0.7723[a]	0.9843[a]	0.5729[a]	0.7195[a]	0.6096[a]	0.9976[a]	0.8533[a]	0.5625[a]	0.7175[a]
ResUNet	0.4939[a]	0.6113[a]	0.9784[a]	0.3700[a]	0.5235[a]	0.4575[a]	0.9968[a]	0.7663[a]	0.4009[a]	0.5708[a]
UNet++	0.6826[a]	0.7605[a]	0.9847[a]	0.5630[a]	0.7094[a]	0.6141[a]	0.9976[a]	0.8532[a]	0.5545[a]	0.7106[a]
AttUNet	0.6847[a]	0.7766[a]	0.9857[a]	0.5743[a]	0.7203[a]	0.6131[a]	0.9973[a]	0.8424[a]	0.5496[a]	0.7064[a]
SegNet	0.6951[a]	0.8032[a]	0.9851[a]	0.5978[a]	0.7394[a]	0.6096[a]	0.9977[a]	0.8636[a]	0.5547[a]	0.7105[a]
PSPNet	0.4115[a]	0.4140[a]	0.9682[a]	0.2420[a]	0.3766[a]	0.4771[a]	0.9874[a]	0.5152[a]	0.3252[a]	0.4873[a]
SegFormer	0.7210	0.8440[a]	0.9880	0.6349	0.7707	0.6399[a]	0.9933[a]	0.7398[a]	0.5530[a]	0.7070[a]
EDA-UNet (Ours)	0.7525	0.8271	0.9887	0.6520	0.7829	0.6943	0.9982	0.8960	0.5931	0.7408

IoU, intersection over union.
[a]Comparison with EDA-UNet model, $p < 0.05$.

Table 4. Quantitative comparison of different models in the task of lipid plaque segmentation

	Internal test					External test				
Models	Sensitivity	Specificity	Accuracy	IoU	Dice coefficient	Sensitivity	Specificity	Accuracy	IoU	Dice coefficient
U-Net	0.6751[a]	0.6889[a]	0.9968	0.5135[a]	0.6751[a]	0.6727[a]	0.9831	0.6564[a]	0.4951[a]	0.6606[a]
ResUNet	0.4940[a]	0.5194[a]	0.9955[a]	0.3316[a]	0.4940[a]	0.4734[a]	0.9831	0.5769[a]	0.3487[a]	0.5165[a]
UNet++	0.6690[a]	0.6992[a]	0.9969	0.5066[a]	0.6690[a]	0.6499[a]	0.9832	0.6498[a]	0.4790[a]	0.6462[a]
AttUNet	0.6777[a]	0.7137[a]	0.9969	0.5171[a]	0.6770[a]	0.6574[a]	0.9842	0.6667[a]	0.4920[a]	0.6581[a]
SegNet	0.7024[a]	0.7192[a]	0.9973	0.5453[a]	0.7023[a]	0.6689[a]	0.9829[a]	0.6536[a]	0.4921[a]	0.6572[a]
PSPNet	0.4908[a]	0.4743[a]	0.9907[a]	0.3287[a]	0.4908[a]	0.5360[a]	0.9760[a]	0.5228[a]	0.3579[a]	0.5262[a]
SegFormer	0.7557[a]	0.7742[a]	0.9971	0.6122[a]	0.7557[a]	0.7254[a]	0.9757[a]	0.6067[a]	0.5121[a]	0.6727[a]
EDA-UNet (Ours)	0.7845	0.7932	0.9975	0.6512	0.7845	0.7666	0.9847	0.6946	0.5480	0.7052

IoU, intersection over union.
[a]Comparison with EDA-UNet model, $p < 0.05$.

coronary artery plaque segmentation. Specifically, the proposed model achieved a MIoU of 0.7849, which was slightly higher than the average performance of senior experts (MIoU = 0.7770) and markedly outperformed junior clinicians (MIoU = 0.7209) and residents (MIoU = 0.6956). Additionally, the proposed model's Dice coefficient of 0.8689 was slightly higher than that of senior experts (Dice coefficient = 0.8499) and significantly outperformed junior clinicians (Dice coefficient = 0.8041) and residents (Dice coefficient = 0.7820). In terms of sensitivity, specificity, and accuracy, the proposed model also demonstrated a notable advantage over clinicians (Table 6).

Notably, in terms of efficiency, the mean times required by residents, junior clinicians, and senior experts to complete the evaluation of all images in each IVOCT pullback was 4.2 h, 3.3 h, and 1.6 h, respectively. In contrast, the EDA-UNet model required only 18 s to complete the evaluation, highlighting its potential for clinical application (Table 6).

DISCUSSION

In this study, the main findings are as follows. (1) An EDA-UNet model was developed and validated for rapid segmentation and quantification of coronary plaques in IVOCT images. In the external test dataset, the overall plaque segmentation achieved a MIoU of 0.7849 and a Dice coefficient of 0.8689, outperforming existing state-of-the-art image segmentation models and previous studies. (2) The EDA-UNet model also demonstrated strong correlation (TCFA: Phi correlation = 0.79, $p < 0.001$; calcification score: $r = 0.95$, $p < 0.001$) and consistency (TCFA: Cohen's Kappa = 0.81, $p < 0.001$; calcification score: weighted Kappa = 0.89, $p < 0.001$) with the ground truth when simultaneously quantitatively evaluating TCFA lesions and assessing calcification score of calcified plaques.

In the external test dataset, the overall quantitative assessment of the EDA-UNet model's performance on the plaque tissue segmentation task was marginally lower than in the internal test dataset; nevertheless, it demonstrated satisfactory performance (Table 1). This result is partly attributed to the low intra-observer and inter-observer variability among the three analysts (Figure S1), highlighting the high reliability of the ground truth annotations. In addition, the internal dataset incorporated multi-source data from two independent medical centers (Figure 7). Although histological analysis of coronary artery pathology is regarded as an ideal ground truth, its small sample size and limited representativeness have hindered its application in DL research. In this study, expert annotations were utilized as the ground truth, and data

Table 5. Quantitative comparison of models from different studies

Studies	Images in the dataset	Categories of labels	MIoU	Dice coefficient
Li[21] (2022)	13,844	calcified plaque	–	0.7560
Chu[22] (2021)	11,673	fibrous, calcified, and lipid plaque, cholesterol crystals, macrophage, microvessel, guidewire, side branch	–	0.7640
Ren[23] (2023)	22,210	fibrous, calcified, and lipid plaque, normal tissue	–	0.7750
Lee[24] (2019)	4,892	fibrolipidic plaque, fibrocalcific plaque	–	0.8140
Tang[25] (2023)	2,388	Calcified and lipid plaque, lumen	–	0.6615
Wang[26] (2023)	5,624	fibrous, calcified, and lipid plaque	0.7497	–
EDA-UNet (Ours)	9,645	fibrous, calcified, and lipid plaque, lumen, guidewire, catheter	0.7849	0.8689

MIoU, mean intersection over union.

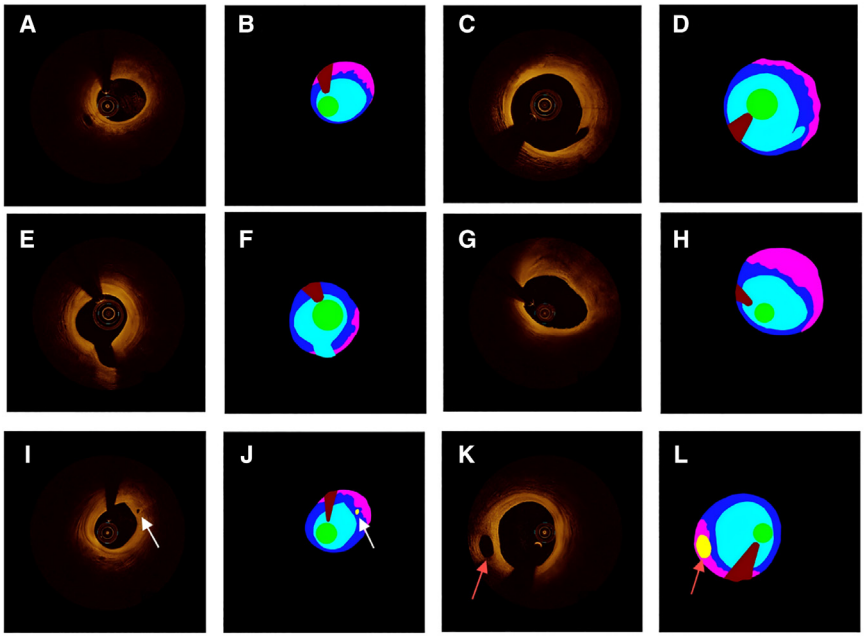

Figure 1. Challenging and failure cases of automatic IVOCT image segmentation

(A–H) Images of the model successfully segmenting challenging cases. (A and B) represent before and after segmentation of residual blood images caused by incomplete rinsing. (C and D) represent coronary artery dissection images before and after segmentation. (E and F) represent branch vessel images before and after segmentation. (G and H) represent extremely eccentric catheter images before and after segmentation.

(I–L) Images of cases in which the model fails to perform accurate segmentation. (I and J) represent microvessel images before and after segmentation. (K and L) represent images of branch vessel that do not intersect the lumen before and after segmentation. The microvessel has been erroneously segmented as calcified plaque (white arrow). The branch vessel that does not intersect the lumen has been incorrectly segmented into calcified plaque (red arrow).

from two independent medical centers were integrated to develop an internal dataset. The extensive real-world dataset encompassed diverse image qualities and demographic features (Table 7), which significantly enhanced the dataset's representativeness and improved the model's generalization capabilities. Notably, the EDA-UNet model was trained on a filtered training dataset. For some special scenarios in IVOCT images, such as large amounts of residual blood in the lumen, bubble artifacts, thrombus in the lumen, eccentric lesions with artifacts, and non-uniform rotational distortion (NURD),[28] the lack of arterial lumen and plaque features behind the artifacts made it difficult for analysts to accurately annotate these areas. Thus, these images were excluded from the training dataset. However, even in complex clinical scenarios, such as a small amount of residual blood in the lumen (Figures 1A and 1B), coronary plaque dissection (Figures 1C and 1D), branching vessels (Figures 1E and 1F), and extremely eccentric catheter (Figures 1G and 1H), the EDA-UNet model was able to accurately segment coronary artery plaques, showcasing exceptional performance and substantial clinical utility. Some relatively rare IVOCT images, such as microvessels (Figures 1I and 1J) or branching vessels disconnected from the lumen (Figures 1K and 1L), exhibited high-attenuation regions with well-defined edges, and were easily misclassified as calcified plaques. The limited number of such images posed challenges for the model in feature extraction, thereby affecting its ability to accurately identify these structures. The segmentation

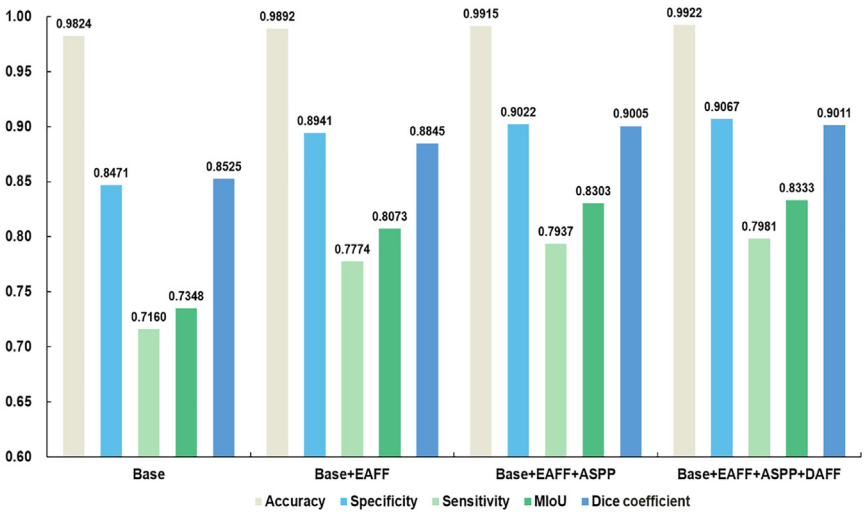

Figure 2. Ablation experiments for the proposed model

MIoU, mean intersection over union.

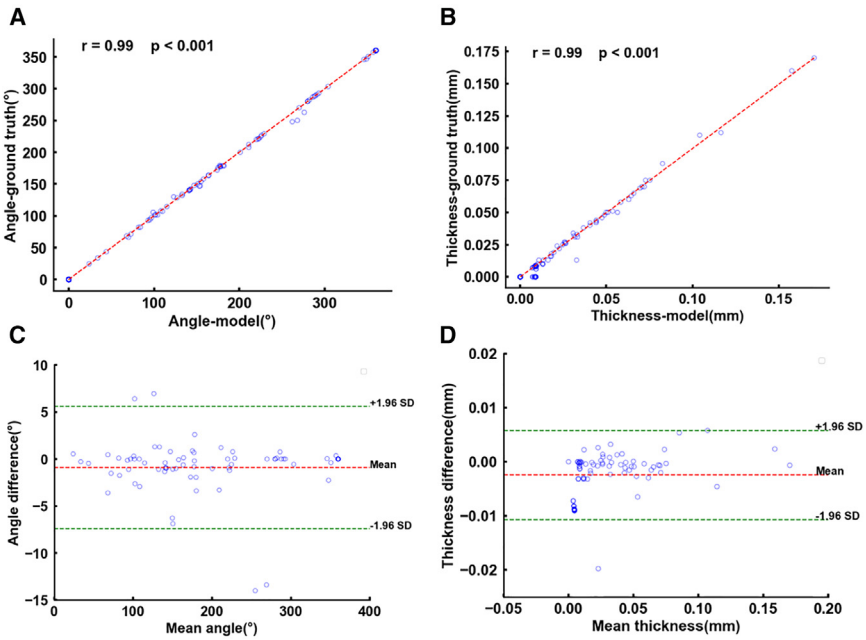

Figure 3. Correlation and consistency between the maximum lipid angle and minimum fibrous cap thickness between the proposed model and ground truth

Correlation of maximum lipid angle (A), Bland-Altman analysis of maximum lipid angle (C), correlation of minimum fibrous cap thickness (B), and Bland-Altman analysis of minimum fibrous cap thickness (D).

performance of the model could have been improved by expanding the dataset or introducing generative adversarial networks.[29]

The performance of the EDA-UNet model was evaluated against several widely used medical image segmentation models, including U-Net,[30] UNet++,[31] ResUNet,[32] AttUNet,[33] SegNet,[34] PSPNet,[35] and Segformer.[36] The comparison results indicated that EDA-UNet model outperformed other state-of-the-art network models in overall quantitative assessment for coronary artery plaque tissue segmentation. In terms of key metrics such as sensitivity, specificity, accuracy, MIoU, and Dice coefficient, EDA-UNet model achieved values of 0.8620, 0.8889, 0.9875, 0.7849, and 0.8689, respectively, in the external test dataset (Table 1). This represented a significant performance advantage over the SegFormer model, with improvements of 0.0033, 0.0607, 0.0023, 0.0449, and 0.0308 for each metric. Although in the quantitative analysis of positive samples (calcified plaque, fibrous plaque, and lipid plaque), some metrics did not show significant improvement (Tables 2, 3, and 4). A visual comparison demonstrated that EDA-UNet exhibited superior performance in processing local details (Figure 8). This was mainly due to the efficient extraction of edge and texture features by the EDA-UNet model. SegFormer, which incorporated a transformer structure, was excellent at extracting global contextual information but relatively weak in processing edge and texture features. Additionally, the transformer structure was relatively insensitive to low-contrast features, making it less efficient than convolutional networks for segmenting diseased tissue. Since the pixel distributions of calcified, fibrous, and lipid plaques accounted for only 1.7%, 5.38%, and 4.1% of the total pixels (Table S1), the quantitative differences between the models were relatively small. As demonstrated in visual comparisons (Figure 8), the segmentation results of the EDA-UNet model in these categories exhibited greater refinement and accuracy. This further highlighted the significant advantages of the EDA-UNet model in processing local details and low-contrast features. In this study, although U-Net, UNet++, ResUNet, AttUNet, SegNet, PSPNet, and EDA-UNet were all based on convolutional neural network architectures, the EDA-UNet model demonstrated significant advantages in both quantitative and visual analyses. This superiority was attributed to its unique design, including the EAFE module, which comprised encoded feature fusion (EFF) and attention feature fusion (AFF) units. The module enhanced the encoder-decoder structure and refined cross-layer connections. By enabling fine-grained cross-scale information transfer, the EAFE module enhanced the EDA-UNet model's focus on segmentation targets while effectively reducing redundant information. Additionally, the EAFE module utilized a combination of deep feature flow (DFF) and AFF units with convolutional kernels of multiple scales to address feature differences within patches, providing the model with superior scale reduction and detail processing capabilities, ultimately optimizing patch segmentation visualization. The ASPP module further enriched semantic information by capturing multi-scale perception fields, thereby enhancing the comprehensive extraction of intravascular tissue integrity across multiple scales. The improved loss function also played a critical role by effectively balancing the proportion between segmentation

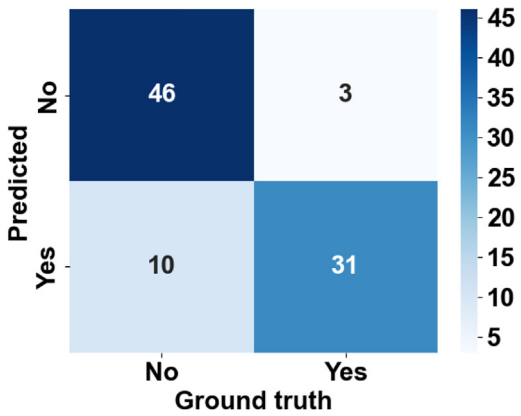

Figure 4. Confusion matrix for comparing the proposed model-identified TCFA with the ground truth (n = 90)

TCFA, thin-cap fibroatheroma.

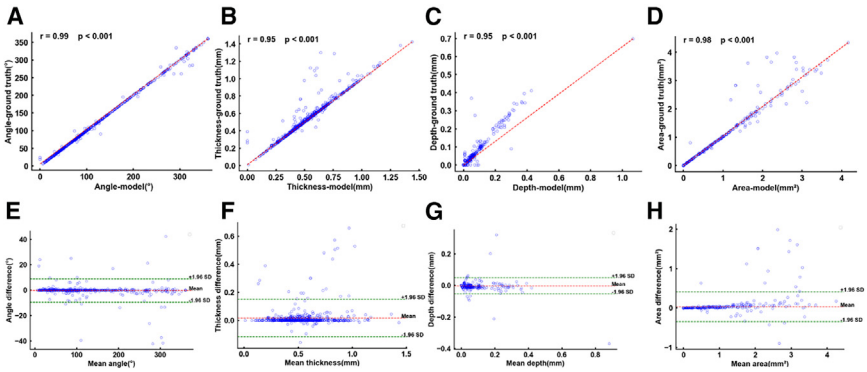

Figure 5. Correlation and consistency of calcification angle, calcification thickness, calcification depth, and calcification area between the proposed model and ground truth

Correlation of calcification angle (A), Bland-Altman analysis of calcification angle thickness (E), correlation of calcification thickness (B), Bland-Altman analysis of calcification thickness (F), correlation of calcification depth (C), Bland-Altman analysis of calcification depth (G), and correlation of calcification area (D), and Bland-Altman analysis of calcification area (H).

targets and the background, improving prediction accuracy and preserving edge details across different categories. Notably, the EDA-UNet method successfully addressed challenges such as fuzzy boundaries between fibrous and lipid plaques and the unclear demarcation between calcified plaques and the background, substantially improving the accuracy of tissue boundary segmentation. In the segmentation task of different plaque types, the proposed model achieved higher segmentation performance for fibrous plaques compared to calcified and lipid plaques, with Dice coefficients of 0.8282, 0.7408, and 0.7052, respectively. Fibrous plaques typically exhibit homogeneous low attenuation coefficient regions, calcified plaques display heterogeneous high attenuation coefficient regions with clear boundaries, and lipid plaques exhibit homogeneous high attenuation coefficient regions with blurred borders in the IVOCT images. The consistent structural characteristics of fibrous plaques are likely the reason that the model achieved higher segmentation accuracy for this plaque type. This variation in segmentation performance across plaque types is consistent with previous findings.[22,37] In summary, the high accuracy and exceptional performance of the EDA-UNet model in segmenting key coronary artery plaque structures were validated, offering a reliable solution for automated IVOCT image segmentation.

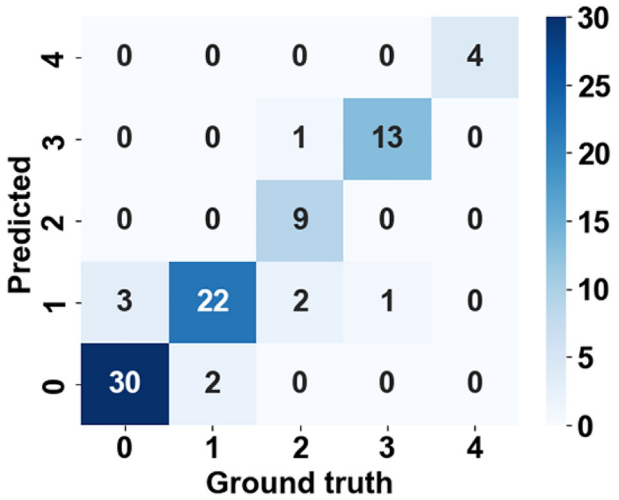

Figure 6. Confusion matrix comparing the proposed model-predicted calcification scores with the ground truth (*n* = 87)

The grading of the calcification score (0, 1, 2, 3, 4) in the graph is usually used to indicate different degrees of calcification, from no calcification to severe calcification, with larger numbers indicating more severe calcification. And the calcium score was defined as follows[27]: 1 point for a maximum calcium thickness >0.5 mm, 2 points for a maximum calcium angle >180°, and 1 point for a calcium length >5 mm.

A few previous studies have attempted to develop models for plaque segmentation in IVOCT. Although there was no direct access to the model code and original datasets of these studies, a visual comparison of their results showed that our proposed model performed better in terms of segmentation performance (Table 6). In addition, most of the previous studies validated their models mainly based on internal datasets and lacked independent external validation, thus the generalization ability of the models is unclear. Among them, Chu et al.[22] used pseudo-3D models to achieve automatic segmentation of plaques, a reasonable strategy given the inherently three-dimensional nature of IVOCT scans. However, the training process of 3D DL models is extremely demanding on computational resources, which requires a large amount of graphics processing unit (GPU) memory and longer processing time. In contrast, our proposed model can achieve comparable segmentation performance based on a frame-by-frame 2D approach. This approach not only significantly reduces the computational resource requirement but also provides more flexibility and applicability for other researchers, especially for scenarios with limited hardware resources. Encouragingly, the EDA-UNet model not only excelled in plaque segmentation performance but also demonstrated the ability to simultaneously quantify the degree of plaque calcification and identify TCFA, a capability that was not available in previous studies. The combined analysis of calcification score and TCFA helped clinicians to quickly assess the degree of calcification in the offender vessel during coronary intervention and accurately identify the presence of TCFA, thus allowing for more precise and optimized intervention strategies.

IVOCT provided clinicians with detailed morphological and risk information about atherosclerotic plaques, making it an indispensable tool in clinical practice.[5,38] However, manual annotation and quantification of plaques in IVOCT images by clinicians remained time-consuming and subjective processes, as

Table 6. Comparison of the performance of the EDA-UNet model with that of clinicians in a reader study

Reader	Sensitivity	Specificity	Accuracy	MIoU	Dice coefficient	Time
Resident 1	0.7877	0.8376	0.9732	0.6919	0.7788	4.0 h
Resident 2	0.7998	0.8370	0.9740	0.6993	0.7852	4.4 h
Junior clinician 1	0.8343	0.8312	0.9779	0.7244	0.8067	2.9 h
Junior clinician 2	0.8328	0.8595	0.9839	0.7173	0.8015	3.7 h
Senior expert 1	0.8888	0.8718	0.9849	0.7828	0.8541	1.8 h
Senior expert 2	0.8855	0.8595	0.9839	0.7712	0.8456	1.4 h
Mean values of residents	0.7938	0.8373	0.9736	0.6956	0.7820	4.2 h
Mean values of juniors	0.8336	0.8454	0.9809	0.7209	0.8041	3.3 h
Mean values of experts	0.8872	0.8657	0.9844	0.7770	0.8499	1.6 h
EDA-UNet (Ours)	0.8620	0.8889	0.9875	0.7849	0.8689	18 s

MIoU, mean intersection over union.

they were prone to high intra-observer and inter-observer variability and required substantial clinical expertise and professional skills.[39] The reader study demonstrated that the EDA-UNet model achieved prediction performance comparable to expert manual labeling while significantly reducing the required time (Table 6). By implementing the EDA-UNet model, the quality and efficiency of medical services were greatly enhanced by significantly reducing the time and effort required for image interpretation and lesion measurement. This enabled clinicians to focus on comprehensive patient health management and surgical processes, thereby ensuring patient safety during percutaneous coronary intervention. In addition, the proposed model provided image interpretation capabilities comparable to those of experts, offering a feasible solution to address the inequality of health services in remote areas and primary care institutions. Since IVOCT images exhibited complex and variable characteristics, and the traditional interpretation process demanded extensive learning and training, the proposed model might serve as a robust self-learning tool for early-career clinicians.

In summary, a pixel-level semantic segmentation model (EDA-UNet) was developed based on a DL neural network. The EDA-UNet model demonstrated strong performance in segmenting various plaque tissues, accurately quantifying calcification score, and evaluating TCFA lesions. The accuracy and robustness of the proposed model have been validated on the external dataset, showing diagnostic performance that surpasses previous DL

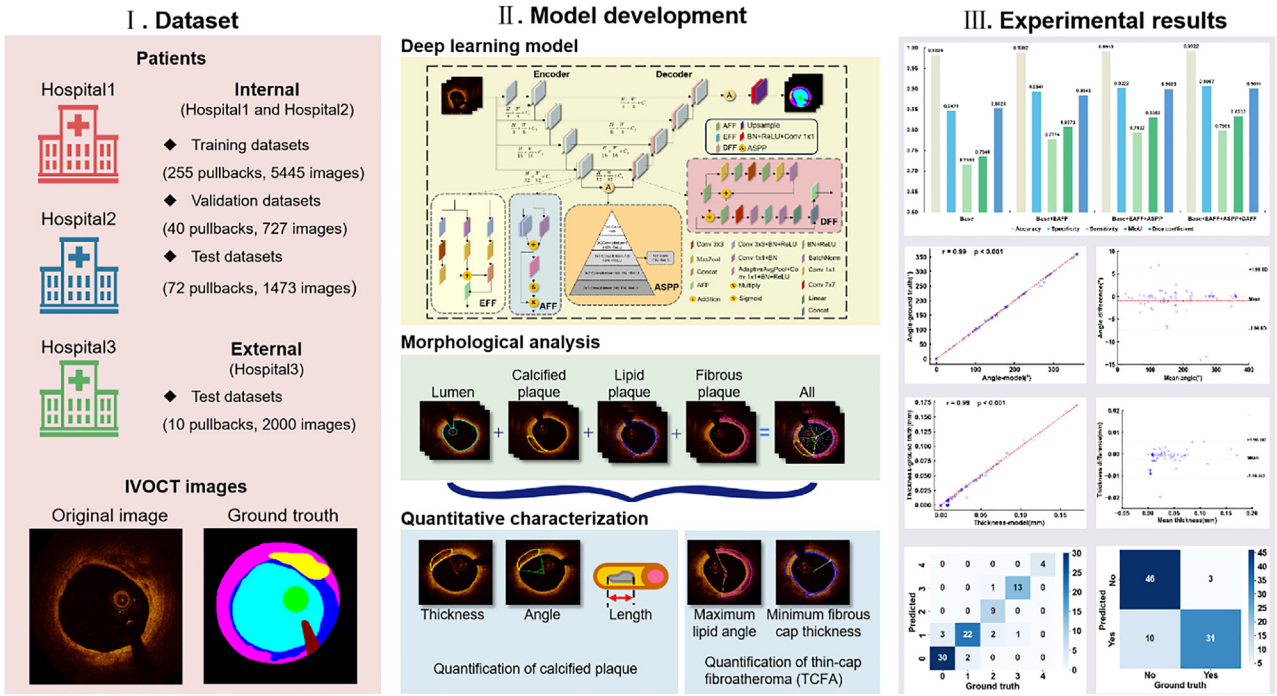

Figure 7. Flowchart of the study design for the development and evaluation of the EDA-UNet model

Table 7. Characteristics of the internal dataset and external dataset

Characteristic	Internal dataset	External dataset
Number of IVOCT images	7,645	2,000
Age (years), mean ± SD	63.30 ± 11.10	62.50 ± 10.30
Sex (female, %)	23.00%	27.50%
Number of pullbacks	367	10
Collection device	C7-X frequency domain OCT system and F-1 frequency domain OCT system	C7-X frequency domain OCT system

Qualitative variables are presented in n (%) and quantitative variables are in mean ± SD. SD, standard deviation.

algorithms and human experts. In the future, the clinical applicability of this model requires further validation through prospective, multicenter studies to enable its broader adoption in clinical practice.

Limitations of the study

Although the EDA-UNet model developed in this study achieved significant results in terms of usability and robustness, there are still some limitations. First, the dataset used in this study was primarily derived from the Chinese population. To promote the global application of the model, data from other ethnicities and regions should be introduced in future studies to validate the model, an essential step toward broad applicability. Second, ethical restrictions limited access to *ex vivo* coronary artery tissue specimens, preventing the use of *ex vivo* pathology as the ground truth for model validation. However, this study used expert image annotation based on consensus guidelines as an alternative, a widely recognized and reliable validation standard in peer-reviewed studies. Third, this study did not classify mixed lesions separately but instead focused on a semantic segmentation model for IVOCT images of fibrous plaques, calcified plaques, and lipid plaques. This approach may have revealed

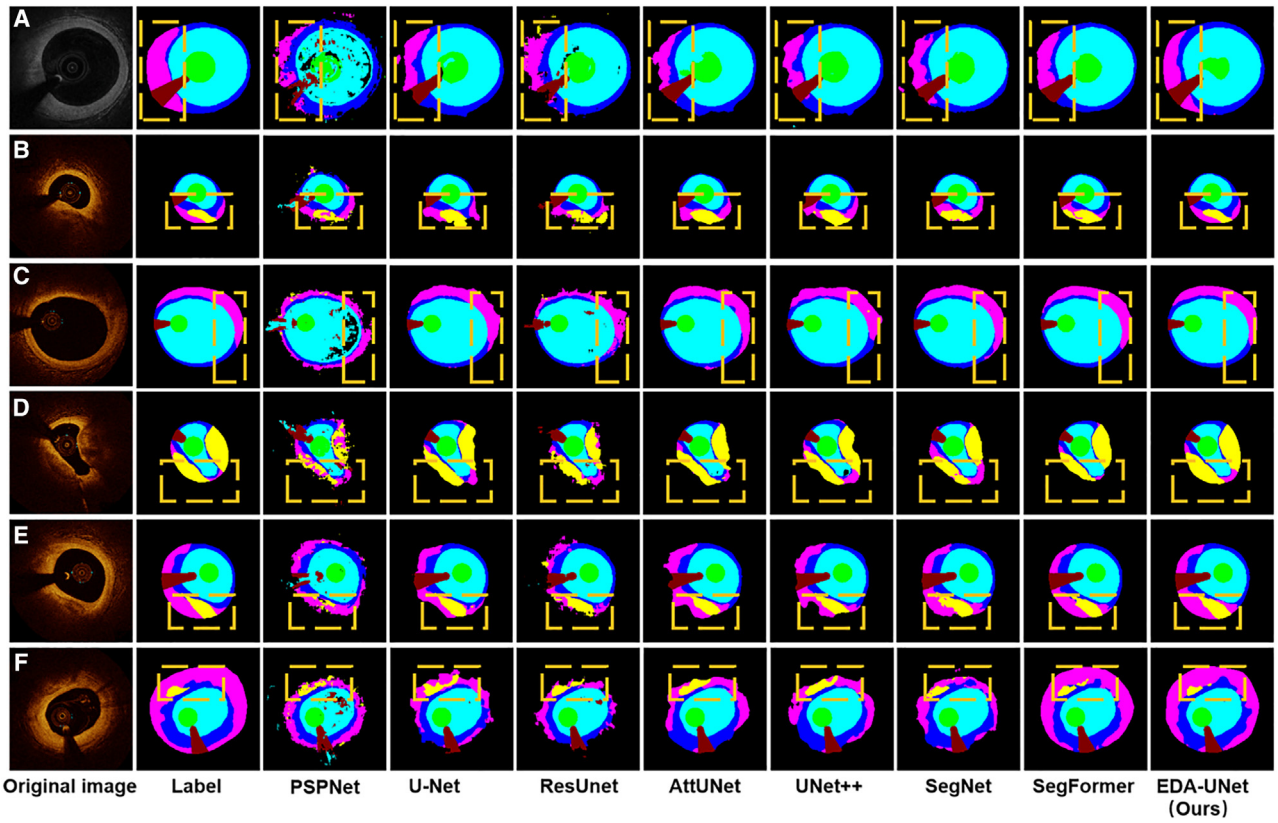

Figure 8. Performance comparison of the proposed model with state-of-the-art network models

The calcified plaques in the yellow boxes of the (B), (E), and (F) rows exhibit a high degree of visual similarity to the background, complicating their differentiation and extraction. In the yellow boxes of the (A) and (C) rows, the outer boundaries of the lipid plaques are difficult to determine, with punctate fibrous plaques and calcified plaques observed inside the lipid plaques, further complicating plaque identification and segmentation. In the yellow box in the (D) row, punctate lipid plaques are scattered within the fibrous plaques, challenging the accurate extraction of intravascular tissue.

limitations in the model's generalizability and clinical applicability. Although mixed lesions are composed of three plaque tissue types, they exhibit blurred boundaries and transitional properties. Individually labeling mixed lesions would necessitate artificially defined boundary thresholds, which often depend on imaging conditions, histopathological criteria, or experimental design and often lack standardization. Soft labeling, multi-category probabilistic labeling, and incorporating a multi-task learning framework might enhance the model's capacity to detect mixed lesions and improve its robustness. Finally, although the dataset used in this study was collected from multiple centers and is therefore relatively diverse, it also contained a small number of challenging images (e.g., large amounts of residual blood in the lumen, bubble artifacts, thrombus in the lumen, eccentric lesions with artifacts, and NURD) that were excluded because the model struggled to learn the characteristics of the lesions due to the absence of arterial lumen and plaque features behind the artifacts. Future research should include more real-world data, particularly from complex scenes, and enhance artifact restoration techniques to improve the model's generalization capability and clinical applicability.

RESOURCE AVAILABILITY

Lead contact

Further information and requests for resources should be directed to and will be fulfilled by the lead contact, Xiang Ma (maxiangxj@yeah.net).

Materials availability

This study did not generate new unique reagents.

Data and code availability

- Due to hospital regulations and patient privacy issues, the IVOCT data reported in this study cannot be stored in a public repository. The anonymized data reported in this article will be shared by the lead contact upon reasonable request.
- All original code has been deposited at https://github.com/lu-cang/EDA-UNet.git and is publicly available as of the date of publication.
- Any additional information required to reanalyze the data reported in this paper is available from the lead contact upon request.

ACKNOWLEDGMENTS

This work was supported by the Key Research and Development Task Special in Xinjiang Uygur Autonomous Region (No. 2022B03022-3), National Natural Science Foundation of China (No. 82360090), and president's fund project of Xinjiang University of political science and law (No. XZZK2023003). The authors acknowledge the clinicians and assistants who participated in this study for data collection, preparation, and quality control. Sincere gratitude to Prof. Lu Xiaolei from Xigu hospital of Lanzhou university second hospital for providing the IVOCT imaging data.

AUTHOR CONTRIBUTIONS

P.L., Z.L., and W.H. contributed to the conception and design, acquisition, analysis, interpretation of the data, drafting of the manuscript and critical revision for important intellectual content. K.K. and C.C. contributed to review & editing, investigation, and interpretation of the data. Z.M. and A.A. completed the software analysis and data visualization. X.P., G.W., and Y.M. collected and organized data. J.D. and X.M. contributed to the conception and design and reviewing of the manuscript or critical revision for important intellectual content. All authors approved the final version, and agree to be accountable for all aspects of the work.

DECLARATION OF INTERESTS

The authors declare no competing interests.

STAR★METHODS

Detailed methods are provided in the online version of this paper and include the following:

- KEY RESOURCES TABLE
- EXPERIMENTAL MODEL AND STUDY PARTICIPANT DETAILS
  - Ethical statement
  - Image datasets
- METHOD DETAILS
  - Development of the EDA-UNet model
  - Evaluation of the EDA-UNet model
  - Reader study
- QUANTIFICATION AND STATISTICAL ANALYSIS

SUPPLEMENTAL INFORMATION

Supplemental information can be found online at https://doi.org/10.1016/j.isci.2025.112169.

Received: September 1, 2024
Revised: December 16, 2024
Accepted: March 3, 2025
Published: March 6, 2025

REFERENCES

1. Tsao, C.W., Aday, A.W., Almarzooq, Z.I., Alonso, A., Beaton, A.Z., Bittencourt, M.S., Boehme, A.K., Buxton, A.E., Carson, A.P., Commodore-Mensah, Y., et al. (2022). Heart Disease and Stroke Statistics—2022 Update: A Report From the American Heart Association. Circulation *145*, e153–e639. https://doi.org/10.1161/CIR.0000000000001052.
2. Roth, G.A., Mensah, G.A., Johnson, C.O., Addolorato, G., Ammirati, E., Baddour, L.M., Barengo, N.C., Beaton, A.Z., Benjamin, E.J., Benziger, C.P., et al. (2020). Global Burden of Cardiovascular Diseases and Risk Factors, 1990-2019: Update From the GBD 2019 Study. J. Am. Coll. Cardiol. *76*, 2982–3021. https://doi.org/10.1016/j.jacc.2020.11.010.
3. Mortensen, M.B., Dzaye, O., Steffensen, F.H., Bøtker, H.E., Jensen, J.M., Rønnow Sand, N.P., Kragholm, K.H., Sørensen, H.T., Leipsic, J., Mæng, M., et al. (2020). Impact of Plaque Burden Versus Stenosis on Ischemic Events in Patients With Coronary Atherosclerosis. J. Am. Coll. Cardiol. *76*, 2803–2813. https://doi.org/10.1016/j.jacc.2020.10.021.
4. Erlinge, D., Maehara, A., Ben-Yehuda, O., Bøtker, H.E., Maeng, M., Kjøller-Hansen, L., Engstrøm, T., Matsumura, M., Crowley, A., Dressler, O., et al. (2021). Identification of vulnerable plaques and patients by intracoronary near-infrared spectroscopy and ultrasound (PROSPECT II): a prospective natural history study. Lancet *397*, 985–995. https://doi.org/10.1016/S0140-6736(21)00249-X.
5. Sarwar, M., Adedokun, S., and Narayanan, M.A. (2024). Role of intravascular ultrasound and optical coherence tomography in intracoronary imaging for coronary artery disease: a systematic review. J. Geriatr. Cardiol. *21*, 104–129. https://doi.org/10.26599/1671-5411.2024.01.001.
6. Bhoite, R., Jinnouchi, H., Otsuka, F., Sato, Y., Sakamoto, A., Kolodgie, F., Virmani, R., and Finn, A. (2020). Ex Vivo assessment of competent strut coverage after coronary stenting by optical coherence tomography. Eur. Heart J. *41*, 2471. https://doi.org/10.1093/ehjci/ehaa946.2471.
7. Martin, W.G., McNaughton, E., Bambrough, P.B., West, N.E.J., and Hoole, S.P. (2023). Interobserver Variability Between Expert, Experienced, and Novice Operator Affects Interpretation of Optical Coherence Tomography and 20 MHz Intravascular Ultrasound Imaging. Cardiovasc. Revasc. Med. *47*, 33–39. https://doi.org/10.1016/j.carrev.2022.09.021.

8. Tearney, G.J., Regar, E., Akasaka, T., Adriaenssens, T., Barlis, P., Bezerra, H.G., Bouma, B., Bruining, N., Cho, J.M., Chowdhary, S., et al. (2012). Consensus standards for acquisition, measurement, and reporting of intravascular optical coherence tomography studies: a report from the International Working Group for Intravascular Optical Coherence Tomography Standardization and Validation. J. Am. Coll. Cardiol. *59*, 1058–1072. https://doi.org/10.1016/j.jacc.2011.09.079.

9. Araki, M., Park, S.J., Dauerman, H.L., Uemura, S., Kim, J.S., Di Mario, C., Johnson, T.W., Guagliumi, G., Kastrati, A., Joner, M., et al. (2022). Optical coherence tomography in coronary atherosclerosis assessment and intervention. Nat. Rev. Cardiol. *19*, 684–703. https://doi.org/10.1038/s41569-022-00687-9.

10. Li, C., Deng, C., Shi, B., and Zhao, R. (2024). Thin-cap fibroatheroma in acute coronary syndrome: Implication for intravascular imaging assessment. Int. J. Cardiol. *405*, 131965. https://doi.org/10.1016/j.ijcard.2024.131965.

11. Jinnouchi, H., Sato, Y., Sakamoto, A., Cornelissen, A., Mori, M., Kawakami, R., Gadhoke, N.V., Kolodgie, F.D., Virmani, R., and Finn, A.V. (2020). Calcium deposition within coronary atherosclerotic lesion: Implications for plaque stability. Atherosclerosis *306*, 85–95. https://doi.org/10.1016/j.atherosclerosis.2020.05.017.

12. Power, D.A., Hemetsberger, R., Farhan, S., Abdel-Wahab, M., Yasumura, K., Kini, A., and Sharma, S.K. (2024). Calcified coronary lesions: Imaging, prognosis, preparation and treatment state of the art review. Prog. Cardiovasc. Dis. *86*, 26–37. https://doi.org/10.1016/j.pcad.2024.06.007.

13. Zhang, R., Fan, Y., Qi, W., Wang, A., Tang, X., and Gao, T. (2022). Current research and future prospects of IVOCT imaging-based detection of the vascular lumen and vulnerable plaque. J. Biophotonics *15*, e202100376. https://doi.org/10.1002/jbio.202100376.

14. Prabhu, D., Bezerra, H., Kolluru, C., Gharaibeh, Y., Mehanna, E., Wu, H., and Wilson, D. (2019). Automated A-line coronary plaque classification of intravascular optical coherence tomography images using handcrafted features and large datasets. J. Biomed. Opt. *24*, 1–15. https://doi.org/10.1117/1.JBO.24.10.106002.

15. Melinscak, M., Radmilovic, M., Vatavuk, Z., and Loncaric, S. (2021). Annotated retinal optical coherence tomography images (AROI) database for joint retinal layer and fluid segmentation. Automatika *62*, 375–385. https://doi.org/10.1080/00051144.2021.1973298.

16. Rico-Jimenez, J.J., Campos-Delgado, D.U., Villiger, M., Otsuka, K., Bouma, B.E., and Jo, J.A. (2016). Automatic classification of atherosclerotic plaques imaged with intravascular OCT. Biomed. Opt. Express *7*, 4069–4085. https://doi.org/10.1364/BOE.7.004069.

17. Ughi, G.J., Adriaenssens, T., Sinnaeve, P., Desmet, W., and D'Hooge, J. (2013). Automated tissue characterization of in vivo atherosclerotic plaques by intravascular optical coherence tomography images. Biomed. Opt. Express *4*, 1014–1030. https://doi.org/10.1364/BOE.4.001014.

18. Chen, T., Yu, H., Jia, H., Dai, J., Fang, C., Ma, L., Liu, H., Xu, M., and Yu, B. (2022). Automatic assessment of calcified plaque and nodule by optical coherence tomography adopting deep learning model. Int. J. Cardiovasc. Imaging *38*, 2501–2510. https://doi.org/10.1007/s10554-022-02637-5.

19. Lee, J., Kim, J.N., Dallan, L.A.P., Zimin, V.N., Hoori, A., Hassani, N.S., Makhlouf, M.H.E., Guagliumi, G., Bezerra, H.G., and Wilson, D.L. (2024). Deep learning segmentation of fibrous cap in intravascular optical coherence tomography images. Sci. Rep. *14*, 4393. https://doi.org/10.1038/s41598-024-55120-7.

20. Liu, Y., Nezami, F.R., and Edelman, E.R. (2024). A transformer-based pyramid network for coronary calcified plaque segmentation in intravascular optical coherence tomography images. Comput. Med. Imaging Graph. *113*, 102347. https://doi.org/10.1016/j.compmedimag.2024.102347.

21. Li, C., Jia, H., Tian, J., He, C., Lu, F., Li, K., Gong, Y., Hu, S., Yu, B., and Wang, Z. (2022). Comprehensive Assessment of Coronary Calcification in Intravascular OCT Using a Spatial-Temporal Encoder-Decoder Network. IEEE Trans. Med. Imaging *41*, 857–868. https://doi.org/10.1109/TMI.2021.3125061.

22. Chu, M., Jia, H., Gutiérrez-Chico, J.L., Maehara, A., Ali, Z.A., Zeng, X., He, L., Zhao, C., Matsumura, M., Wu, P., et al. (2021). Artificial intelligence and optical coherence tomography for the automatic characterisation of human atherosclerotic plaques. EuroIntervention. *17*, 41–50. https://doi.org/10.4244/eij-d-20-01355.

23. Ren, X.B., Zhao, Y.X., Fan, J.B., Wu, H.Y., Chen, Q., and Kubo, T. (2023). Semantic segmentation of superficial layer in intracoronary optical coherence tomography based on cropping-merging and deep learning. Infrared Phys. Technol. *129*, 104542. https://doi.org/10.1016/j.infrared.2022.104542.

24. Lee, J., Prabhu, D., Kolluru, C., Gharaibeh, Y., Zimin, V.N., Bezerra, H.G., and Wilson, D.L. (2019). Automated plaque characterization using deep learning on coronary intravascular optical coherence tomographic images. Biomed. Opt. Express *10*, 6497–6515. https://doi.org/10.1364/BOE.10.006497.

25. Ren, X., Zhao, Y., Fan, J., Wu, H., Chen, Q., and Kubo, T. (2023). Semantic segmentation of superficial layer in intracoronary optical coherence tomography based on cropping-merging and deep learning. Infrared Phys. Technol. https://doi.org/10.1016/j.infrared.2022.104542.

26. Wang, Z., Zheng, J., Jiang, P., and Gao, D. (2023). Sk-Conv and SPP-based UNet for lesion segmentation of coronary optical coherence tomography. Technol. Health Care *31*, 347–355. https://doi.org/10.3233/THC-236030.

27. Fujino, A., Mintz, G.S., Matsumura, M., Lee, T., Kim, S.Y., Hoshino, M., Usui, E., Yonetsu, T., Haag, E.S., Shlofmitz, R.A., et al. (2018). A new optical coherence tomography-based calcium scoring system to predict stent underexpansion. EuroIntervention. *13*, e2182–e2189. https://doi.org/10.4244/EIJ-D-17-00962.

28. Cao, G., Li, S., Zhang, S., Peng, Z., Wu, Y., Wang, D., and Dai, C. (2023). Improved FAST algorithm for non-uniform rotational distortion correction in OCT endoscopic imaging. Opt. Express *31*, 2754–2767. https://doi.org/10.1364/oe.474955.

29. Goodfellow, I., Pouget-Abadie, J., Mirza, M., Xu, B., Warde-Farley, D., Ozair, S., Courville, A., and Bengio, Y. (2020). Generative adversarial networks. Commun. ACM *63*, 139–144. https://doi.org/10.1145/3422622.

30. Tatli, U., and Budak, C. (2023). Biomedical Image Segmentation with Modified U-Net. Trait. Du. Signal *40*, 523–531. https://doi.org/10.18280/ts.400211.

31. Zhou, Z., Siddiquee, M.M.R., Tajbakhsh, N., and Liang, J. (2018). UNet++: A Nested U-Net Architecture for Medical Image Segmentation. Deep Learn. Med. Image Anal. Multimodal Learn. Clin. Decis. Support *11045*, 3–11. https://doi.org/10.1007/978-3-030-00889-5_1.

32. Xu, S., Lu, H., Cheng, S., and Pei, C. (2022). Left Ventricle Segmentation in Cardiac MR Images via an Improved ResUnet. Int. J. Biomed. Imaging *2022*, 8669305. https://doi.org/10.1155/2022/8669305.

33. Bougourzi, F., Distante, C., Dornaika, F., and Taleb-Ahmed, A. (2023). PDAtt-Unet: Pyramid Dual-Decoder Attention Unet for Covid-19 infection segmentation from CT-scans. Med. Image Anal. *86*, 102797. https://doi.org/10.1016/j.media.2023.102797.

34. Yan, Z., Su, Y., Sun, H., Yu, H., Ma, W., Chi, H., Cao, H., and Chang, Q. (2022). SegNet-based left ventricular MRI segmentation for the diagnosis of cardiac hypertrophy and myocardial infarction. Comput. Methods Programs Biomed. *227*, 107197. https://doi.org/10.1016/j.cmpb.2022.107197.

35. Zhu, X., Cheng, Z., Wang, S., Chen, X., and Lu, G. (2021). Coronary angiography image segmentation based on PSPNet. Comput. Methods Programs Biomed. *200*, 105897. https://doi.org/10.1016/j.cmpb.2020.105897.

36. Yu, H., Ye, X., Hong, W., Shi, R., Ding, Y., and Liu, C. (2024). A cascading learning method with SegFormer for radiographic measurement of periodontal bone loss. BMC Oral Health *24*, 325. https://doi.org/10.1186/s12903-024-04079-y.

37. Shibutani, H., Fujii, K., Ueda, D., Kawakami, R., Imanaka, T., Kawai, K., Matsumura, K., Hashimoto, K., Yamamoto, A., Hao, H., et al. (2021). Automated classification of coronary atherosclerotic plaque in optical frequency domain imaging based on deep learning. Atherosclerosis *328*, 100–105. https://doi.org/10.1016/j.atherosclerosis.2021.06.003.

38. Chandramohan, N., Hinton, J., O'Kane, P., and Johnson, T.W. (2024). Artificial Intelligence for the Interventional Cardiologist: Powering and Enabling OCT Image Interpretation. Interv. Cardiol. *19*, e03. https://doi.org/10.15420/icr.2023.13.

39. Garg, M., Garcia-Garcia, H.M., Calderón, A.T., Gupta, J., Sortur, S., Levine, M.B., Singla, P., Picchi, A., Sardella, G., Adamo, M., et al. (2024). Reproducibility of an artificial intelligence optical coherence tomography software for tissue characterization: Implications for the design of longitudinal studies. Cardiovasc. Revasc. Med. *58*, 79–87. https://doi.org/10.1016/j.carrev.2023.07.003.

STAR★METHODS

KEY RESOURCES TABLE

REAGENT or RESOURCE	SOURCE	IDENTIFIER
Deposited data		
Intravascular optical coherence tomography (IVOCT) dataset	This paper	N/A
Software and algorithms		
R (version 4.2.2)	R software	https://www.r-project.org/
ImageJ (version 1.8.0)	ImageJ software	https://imagej.net/ij/
Python (version 3.8.13)	Python software	Welcome to Python.org
UNet	Tatli et al.[30]	https://github.com/Andy-zhujunwen/UNET-ZOO.git
ResUnet	Xu et al.[32]	https://github.com/rishikksh20/ResUnet.git
AttUNet	Bougourzi et al.[33]	https://github.com/bigmb/Unet-Segmentation-Pytorch-Nest-of-Unets.git
UNet++	Zhou et al.[31]	https://github.com/Won6314/UnetPP.git
SegNet	Yan et al.[34]	https://github.com/delta-nera/segnet_pytorch.git
PSPNet	Zhu et al.[35]	https://github.com/Lextal/pspnet-pytorch.git
SegFormer	Yu et al.[36]	https://github.com/lucidrains/segformer-pytorch.git
EDA-UNet	This study	https://github.com/lu-cang/EDA-UNet.git

EXPERIMENTAL MODEL AND STUDY PARTICIPANT DETAILS

Ethical statement

The present study complied with the term of the Declaration of Helsinki and was approved by Institutional Review Board of the First Affiliated Hospital of Xinjiang Medical University (Ethics Approval Number: 240104-02). Participants gave informed consent to participate in the study before taking part. All IVOCT images were irreversibly anonymized.

Image datasets

The current study protocol is illustrated in Figure 7. And this study is a retrospective and multicenter study. The internal dataset consisted of 267 clinical pullbacks provided by the First Affiliated Hospital of Xinjiang Medical University and 100 clinical pullbacks from the Jining No.1 People's Hospital, containing a total of 7,645 IVOCT images representing various plaque tissues (Figure 7). To avoid potential overlap between adjacent images in the same pullback, the dataset was divided into a training set (255 pullbacks, 70%), a validation set (40 pullbacks, 10%), and a test set (72 pullbacks, 20%) based on the pullback level. The external dataset consisted of 10 pullbacks provided by Xigu hospital of Lanzhou university second hospital, totaling 2,000 IVOCT images (Figure 7). For data acquisition, the First Affiliated Hospital of Xinjiang Medical University and Xigu hospital of Lanzhou university second hospital used the C7-X frequency domain OCT system (Abbott, California, USA), while Jining No.1 People's Hospital used the F-1 frequency domain OCT system (Wolfmann Medical, Nanjing, China). Detailed characteristics of the data are presented in Table 7. For the internal dataset, the mean age was 63.30 ± 11.10 years, with 23.00% of participants being female. In the external dataset, the mean age was 62.50 ± 10.30 years, with 27.50% of participants being female. All three centers used non-occlusive technology for data acquisition.

During the annotation of the ground truth for the internal dataset, the plaque components in the IVOCT cross-sectional images were annotated at 2 mm longitudinal intervals (one every 10 frames) per retraction to reduce the prevalence of plaque components with similar textures in the training dataset and enhance sample diversity. For the annotation of external dataset, consecutive IVOCT images in the pullbacks were annotated to concurrently evaluate the proposed model's segmentation and quantification capabilities. During data preparation, poor-quality IVOCT images (e.g., those containing stent struts, large amounts of residual blood in the lumen, bubble artifacts, thrombus in the lumen, eccentric lesions with artifacts and NURD) were excluded from the analysis. Specifically, 253 images (3.3% of the internal dataset) and 57 images (2.8% of the external dataset) were removed. However, the proportion of excluded images is exceedingly small and is unlikely to have a meaningful impact on the quality or representativeness of the overall dataset. To further increase sample diversity, data augmentation was applied by rotating the original images by 90° and 270°. The resolution of the original IVOCT images was 1024 × 1024, but this introduced potential redundancy in the segmentation task by incorporating excessive background information. Following multiple experimental optimizations, we adjusted the image size to 640 × 640 to achieve optimal prediction outcomes.

The ground truth data were generated by two experienced IVOCT analysts (Analyst A: P.F.L. and Analyst B: C.L.) from the Core Laboratory of Xinjiang Medical University using Labelme software and through consensus (Figure S2). The lumen and internal elastic lamina of the coronary arteries were annotated in each IVOCT image using the Cartesian coordinate system, followed by the annotation of other tissues between these structures. Coronary plaque tissue was classified into three categories: fibrous plaque, lipid plaque, and calcified plaque, while nonvascular structures were categorized as guidewires, background, lumens, and IVOCT catheters. In the quantification of calcified plaques, ImageJ software was used to measure the angle, thickness, and length of each calcified lesion segment in the IVOCT images, and a calcification score was calculated accordingly. Scoring criteria were defined as follows: 1 point for a maximum thickness >0.5 mm, 2 points for a maximum angle >180°, and 1 point for a length >5 mm.[27] To more accurately quantify TCFA, the thickness of the thinnest fibrous cap and the maximum lipid angle in each frame of the IVOCT image were measured using ImageJ software. According to expert consensus and related research, TCFA is defined as a maximum lipid angle >90° and a minimum fibrous cap thickness <65μm.[8,9] For the IVOCT image after plaque segmentation, the coordinates of all points in the lumen were obtained, and their average was calculated as the lumen centroid. The diameter of the IVOCT catheter region (2.7F/3 = 0.9 mm) was used as a scale in the segmented coronary artery image. If there were calcified plaques in the image, rays were drawn from the centroid as the origin, and the maximum pixel value of the calcified plaque was taken as its maximum thickness. The angle between the two lines segments formed by connecting the centroid to the two edge points of the calcified plaque represents its angular value. To determine the length of the calcification, the first and last IVOCT frames containing calcification were identified, the number of consecutive frames between them was counted, and the result was multiplied by 0.2 mm. Finally, the angle, thickness, and length of the calcification in these consecutive coronary artery images were calculated, and a score was assigned to the calcification according to the IVOCT calcification scoring system. For each IVOCT image with a lipid pool after segmentation (i.e., the lipid pool spans more than one pixel in the image), rays were drawn from the centroid as the origin, and the minimum pixel distance between the lumen boundary and the inner boundary of the lipid pool was measured. If this minimum value was thinner than 65μm, the lesion at this location was defined as a TCFA.

In cases of disagreement during the analysis, the analysts consulted a senior IVOCT expert (Analyst C: X.M.) to resolve the dispute and reach a final consensus. To assess inter- and intra-analyst variability, 6 pullbacks were randomly selected from the internal dataset and independently labeled by Analysts A, B, and C. One month later, the three analysts independently re-labeled the same samples. Inter-observer variability was evaluated by comparing the annotation results of Analysts A, B, and C, while intra-observer variability was assessed by comparing each analyst's initial annotations with their corresponding annotations one month later (Figure S1).

METHOD DETAILS

Development of the EDA-UNet model

In this study, a model of the EDA-UNet with an encoder-decoder structure was proposed for segmenting IVOCT images (Figure S3). The overall structure of EDA-UNet consisted of three main components: (1) encoder, performing multiscale fusion through skip connections and utilizing the local attention mechanism to enhance focus on important information across different categories; (2) middle layer, employing atrous convolution kernels with varying dilation rates to expand the receptive field and capture broader contextual information; (3) decoder, integrating different features of the same scale through skip connections and extracting same-scale feature information using the local attention mechanism. The model structure was detailed as follows (Figure S3).

Model training was performed using the PyTorch framework on an NVIDIA RTX 3090 GPU. The experimental parameters were kept constant throughout the training process. The training used the stochastic gradient descent optimization algorithm, with an initial learning rate of 0.0001, linear weight decay, a batch size of 3, and a total of 150 epochs. At the 96th epoch, the loss value on the internal validation set reached a local minimum (0.09976), indicating that the model's performance on unseen data was optimal at this point, demonstrating optimal generalization ability. Therefore, we selected the model parameters of the 96th epoch as the final model to maximize predictive accuracy on new data while preserving robust training performance (Figure S4).

Evaluation of the EDA-UNet model

In order to comprehensively evaluate the performance of the EDA-UNet model, comparative experiments were conducted on the test dataset against seven leading state-of-the-art network models in medical image segmentation, including U-Net, ResUNet, UNet++, AttUNet, SegNet, PSPNet, and Segformer. All models used the same training method and were tested on the same dataset to ensure a fair and consistent comparison. To further evaluate the performance of the proposed EDA-UNet model, we compared it with various models from previous IVOCT coronary plaque segmentation studies. Due to the lack of publicly available datasets and source codes from related studies, we conducted our performance comparison based on their reported findings and employed the widely used MIoU and Dice coefficients as evaluation metrics.

To further evaluate the performance of the proposed EDA-UNet model, we conducted a comparison with several models from previous IVOCT coronary plaque segmentation studies. Given that the datasets and source codes from these studies are not publicly accessible, our performance comparison relied on the results reported in each study. We utilized the widely recognized MIoU and Dice coefficients as evaluation metrics to ensure consistency and comparability.

For the purpose of evaluating the effectiveness of individual modules in the EDA-UNet model, ablation experiments were conducted. The semantic segmentation model U-Net was used as the baseline model (Base), with the EAFE module, the ASPP module, and the DAFE module gradually added to assess the contribution of each module to overall model performance.

Building upon its accurate segmentation of coronary artery plaques, the EDA-UNet model's ability to quantify calcification scores and TCFA was validated by comparing its automated measurements with manually annotated ground truth data.

Reader study

With the aim of examining the clinical applicability of the EDA-UNet model, a reader study was conducted on a continuous-frame IVOCT image from an independent pullback in an external dataset. Six clinicians with varying levels of IVOCT diagnostic experience, who were not involved in dataset annotation, participated in this study. They were divided into three groups based on experience: 1–3 years, 5–7 years, and over 10 years. Each clinician independently reviewed the images and provided a diagnosis. The entire process was conducted in a blinded manner to ensure objective and reliable assessment results.

QUANTIFICATION AND STATISTICAL ANALYSIS

The performance of the EDA-UNet model was assessed using several performance metrics: sensitivity, specificity, accuracy, IoU, MIoU, and Dice coefficient. The relationships between these metrics and their parameters were defined by the following formulas:

$$Sensitivity = \frac{TP}{TP+FN} \quad \text{(Equation 1)}$$

$$Specificity = \frac{TN}{TN+FP} \quad \text{(Equation 2)}$$

$$Accuracy = \frac{TP+TN}{TP+TN+FP+FN} \quad \text{(Equation 3)}$$

$$IoU = \frac{TP}{TP+FP+FN} \quad \text{(Equation 4)}$$

$$MIoU = \frac{1}{N}\sum_{i=1}^{N}\frac{TP_i}{TP_i+FP_i+FN_i} \quad \text{(Equation 5)}$$

$$Dice\ coefficient = \frac{2 \times TP}{2 \times TP+FP+FN} \quad \text{(Equation 6)}$$

TP, TN, FP, and FN indicate true positive, true negative, false positive, and false negative, respectively. The performance metrics of the different models were compared using the Wilcoxon signed-rank test (Tables 1, 2, 3, and 4). In addition, agreement between groups for continuous variables was assessed using Bland-Altman analysis (Figures 3C, 3D, and 5E–5H). The agreement between the model predictions and the underlying ground truth for TCFA diagnosis and calcium scores was assessed using Cohen's Kappa analysis (Figure 4) and weighted Kappa analysis (Figure 6), respectively. The Kappa value ranges from 0 to 1, with values greater than 0.8 generally indicating near-perfect agreement. Pearson (Figures 3A, 3B, and 5A–5D), Spearman (Figure 6), or Phi (Figure 4) correlation coefficients were used to assess correlations between ground truth data and model predictions for continuous variables, calcium scores, and TCFA identification, respectively. The correlation coefficient ranges from −1 to 1, and when its absolute value is greater than 0.8, it indicates a strong correlation. Statistical analysis was performed using R software (version 15.2.2), while Python (version 3.8.13) and the DL framework PyTorch (version 1.11.0) were used for model construction and data analysis. All statistical tests were two-sided, and the statistical significance level was set to $p < 0.05$.